THE JOURNAL OF PHYSICAL CHEMISTRY C
A JOURNAL OF THE AMERICAN CHEMICAL SOCIETY

pubs.acs.org/JPCC

Article

Electromechanically Actuated MXene Nanotubes for Tunable Mass Transport

Bozhao Wu,[§] Yuanpeng Yao,[§] Ke Zhou, Ze Liu,* and Enlai Gao*

Cite This: *J. Phys. Chem. C* 2021, 125, 25275−25283

Read Online

ACCESS | Metrics & More | Article Recommendations | Supporting Information

ABSTRACT: Developing stimuli-responsive nanochannels for tunable mass transport has attracted considerable attention. Herein, we investigate the electromechanical actuation of Sc_2C MXene nanotubes (MNTs) that can be rolled from planar Sc_2C and the application of the electromechanically actuated MNTs for tunable mass transport. Our results demonstrate that the maximum radial actuation strain is as high as 26.8% for MNTs upon charge injection while maintaining sufficient structural integrity. The underlying mechanism behind this high actuation performance of MNTs and planar Sc_2C is revealed by atomic- and electronic-scale analyses. Finally, we probe the transport behaviors of a molecule test case (neopentane, C_5H_{12}) passing through electromechanically actuated MNTs and demonstrate that the tunability of sieving diameters endows MNTs with the capability of tunable mass transport. These findings provide a feasible solution for the development of tunable nanochannels.

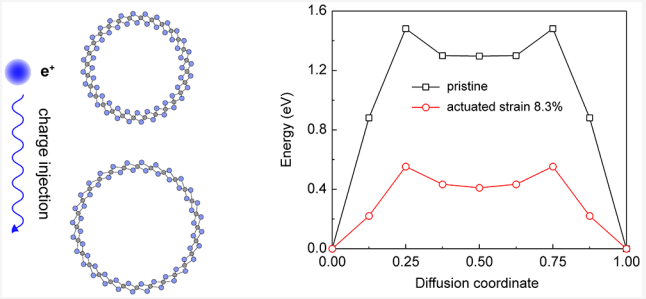

INTRODUCTION

Solid-state actuator materials that convert external stimuli into mechanical responses[1−4] are of practical interest for applications, such as micro- and nanoelectromechanical devices, artificial muscles, robotics, resonators, sensors, and switches. Although developing actuator materials has attracted considerable attention, classical actuator materials, including electroactive ceramics, polymers, and shape memory alloys, have shortcomings, such as small strokes and unpredictable deformation,[5,6] which limit their applications. Electromechanical actuation materials provide a promising route to address this issue.[7−10] For example, Baughman[7] found that carbon nanotube sheets exhibit remarkable actuation performance when immersed in an aqueous electrolyte. Afterward, first-principles calculations predicted dimensional changes of carbon nanotubes as a function of charge injection.[8]

Recently, the discovery of two-dimensional materials (2DMs) has accelerated the development of micro- and nanoscale material-based actuators. The actuation performance of numerous 2DMs, such as graphene and its oxide,[10−12] phosphorene,[13] transition-metal dichalcogenides,[14,15] and MXenes,[16−18] has been investigated by experiments and theoretical calculations. On the experimental side, a graphene-based electromechanical resonator exhibits actuated vibrations with fundamental resonant frequencies in the megahertz range under a direct current voltage.[19] A MXene ($Ti_3C_2T_x$)-based actuator shows changes in curvature and strain up to 0.038 mm^{-1} and 0.26% under a low voltage.[18] On the theoretical side, Liu et al.[12] found that the phase transition in graphene oxide provides a maximum recoverable stroke of 14.5%. More recently, it was predicted that phosphorene exhibits in-plane anisotropic strokes with a maximum actuation strain of 36.6%,[13] while Ti_2C MXene boasts in-plane isotropic strokes with a maximum actuation strain of 27.4%.[16] Recently, experimental evidence demonstrated the formation of scrolls from planar Ti_3C_2,[20] and the stability of MXene nanotubes (MNTs) also has been predicted by density functional theory (DFT) and density functional-based tight binding calculations.[21,22]

Considering that nanotubes can be formed by rolling up 2DMs, we wonder whether nanotubes prepared by rolling up responsive 2DMs would exhibit interesting actuation performance. Moreover, if the diameter of these nanotubes can be changed by an external stimulus, this responsive nanochannel can be highly promising for tunable mass transport. Tunable mass transport is of fundamental importance not only in separation-based applications[23−25] but also in biological sensing,[26] drug delivery,[27,28] catalysis,[29,30] nanofluidics,[31,32] proton transport,[33] and energy harvesting.[34] Responsive nanochannels with tunable sieving diameters are the best candidates for such applications.[35−37] To date, stimuli, such as heat,[38] environmental pH,[39,40] ions/molecules,[41,42] and light,[43]

Received: August 22, 2021
Revised: October 18, 2021
Published: November 4, 2021

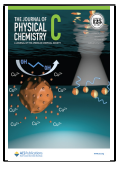

https://doi.org/10.1021/acs.jpcc.1c07453
J. Phys. Chem. C 2021, 125, 25275−25283

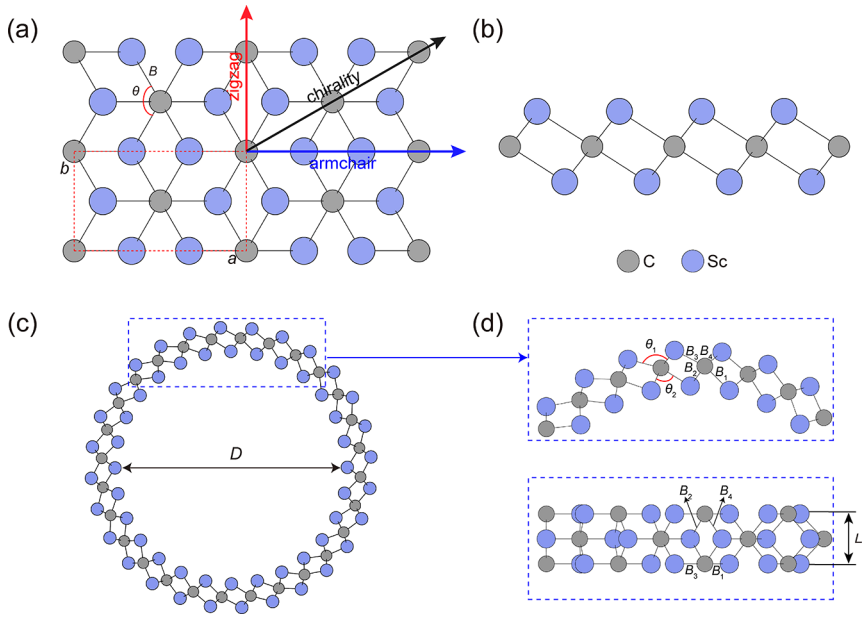

Figure 1. Structures of planar Sc_2C and MNTs. (a,b) Top and side views of planar Sc_2C with the unit cell in the red dashed lines. (c,d) Side and top views of MNT-14. D, L, B_{1-4}, and θ_{1-2} are the diameter, axial length, bond length, and angle of MNT-14, respectively. Panel (d) provides the enlarged side and top views of panel (c) within the blue dashed lines.

Table 1. Structural Parameters of MNTs

MNTs	D (Å)	L (Å)	B_1 (Å)	B_2 (Å)	B_3 (Å)	B_4 (Å)	θ_1 (deg)	θ_2 (deg)
MNT-6	9.02	3.42	2.24	2.37	2.35	2.23	116.74	77.66
MNT-10	16.12	3.33	2.28	2.35	2.28	2.21	109.17	81.60
MNT-14	23.30	3.31	2.29	2.33	2.26	2.21	105.30	83.91

have been used to produce controllable responses of nanochannels, but challenges remain, particularly in terms of stimulus complexity (e.g., solutions and ions) and response uncontrollability (e.g., low durability and response rate).[36]

Herein, we computationally investigate the actuation performance of Sc_2C MNTs in response to charge injection. Our results show that MNTs exhibit high electromechanical actuation performance with a maximum radial actuation strain of 26.8% while maintaining sufficient structural integrity under electromechanical loads. Insights into atomic and electronic structures reveal the underlying mechanism for this behavior. Finally, we demonstrate that the tunability of the diameter endows MNTs with the capability of tunable mass transport by passing a molecule (C_5H_{12}) through an MNT with various actuated diameters.

COMPUTATIONAL METHODS

First-principles calculations were performed under the framework of DFT as executed in the Vienna ab initio simulation package.[44,45] The generalized gradient approximation[46] of the Perdew–Burke–Ernzerhof functional[47] was used for the exchange and correlation interactions of electrons. Projector augmented wave potentials were used to treat ion-electron interactions.[48] Considering the dispersion interactions, van der Waals corrections using the DFT-D3 method were adopted in all calculations.[49] Monkhorst–Pack grid k-points[50] with densities greater than 40 Å were used for Brillouin zone sampling. The convergence test was performed to verify the rationality of the selected energy cutoff. Figure S1c,d demonstrates that the energy cutoff of 400 eV provides a good balance between computational accuracy and cost for the calculations of the electromechanical performance of planar Sc_2C and MNTs. Hence, the energy cutoff was set at 400 eV in all the calculations. All structures were fully relaxed using a conjugate gradient algorithm with a convergence criterion less than 0.01 eV/Å for the force on each atom. On calculating the electromechanical actuation performance of planar Sc_2C and MNTs, the injected charges were compensated using a jellium background charge to maintain charge neutrality in the computational cell. Unless otherwise noted, a vacuum layer of thickness greater than 70 Å was adopted to eliminate electrostatic interactions.[13,16]

RESULTS AND DISCUSSION

Structures of Planar Sc_2C and MNTs. Similar to rolling up graphene sheets into carbon nanotubes, MNTs can be constructed by rolling up planar Sc_2C (Figure 1a,b). Specifically, structural optimization was performed on the unit cell of planar Sc_2C within the red dashed lines, which yields lattice parameters a = 5.71 Å and b = 3.30 Å and interatomic parameters B = 2.26 Å and θ = 93.59°. Afterward, 6 × 1, 10 × 1 and 14 × 1 supercells of planar Sc_2C are constructed and rolled into MNTs with diameters of 0.9–2.3 nm, named MNT-6, MNT-10, and MNT-14, respectively (Figures 1c and S1a,b). Unless otherwise mentioned, the diameter of an MNT refers to its inner diameter (D), as illustrated in Figure 1c. Table 1 lists the structural parameters of MNT-6, MNT-10, and MNT-14 (Figure 1c,d). In contrast to uniform bond length and angle of planar Sc_2C, the bond length (B_{1-4}) and angle (θ_{1-2}) of MNTs alternate, since bending-induced tension in the outer atomic layer and compression in the inner atomic layer of MNTs disrupt the

https://doi.org/10.1021/acs.jpcc.1c07453
J. Phys. Chem. C 2021, 125, 25275–25283

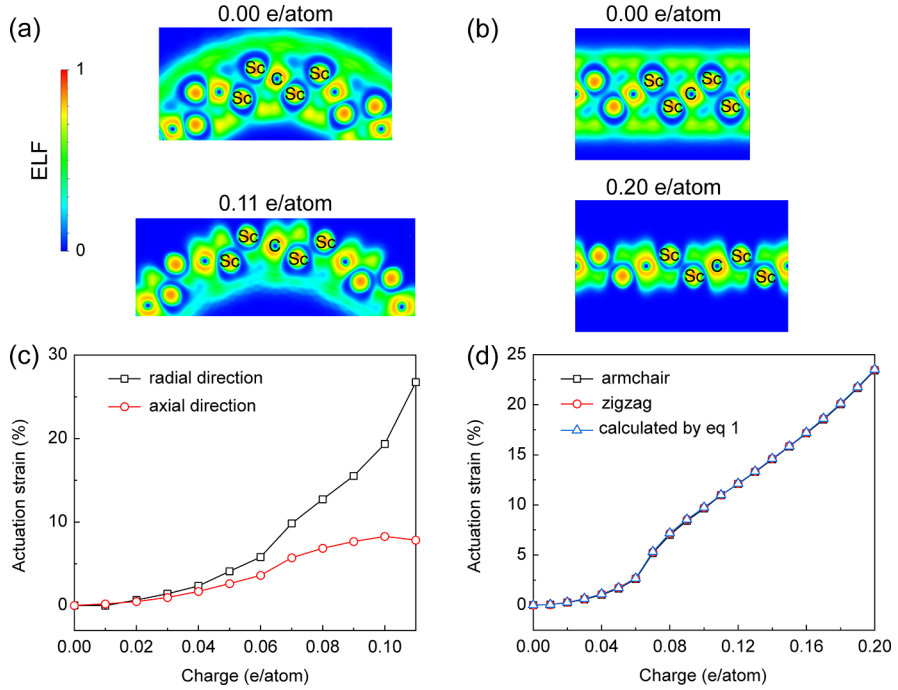

Figure 2. Plotted ELF graphs of (a) MNT-14 and (b) planar Sc_2C before and after charge injection. The ELF graph of MNT-14 shown on the cross-sectional plane with the distance of L from the origin. For planar Sc_2C, the ELF graph of a supercell ($3 \times 1 \times 1$) shown on the (010) plane with a distance of lattice b from the origin. (c,d) Actuation performance of MNTs and planar Sc_2C in response to charge injection. (c) Radial and axial actuation strain of an MNT-14 and (d) actuation strain of a planar Sc_2C along the armchair and zigzag directions.

symmetry of planar Sc_2C.[16] In addition, this alternation of the bond length and angle decreases as the bending of the MNTs decreases (Table 1). Considering the thermodynamics, ab initio molecular dynamics (AIMD) simulations were carried out to investigate the stability of MNTs. The temperature of 298 K was controlled using an Andersen thermostat. During the whole AIMD simulations of 10 ps, the evolution of temperature and system energy is gentle (Figure S2a) and the MNT upholds its structural integrity with only slight corrugation because of thermal fluctuation (Movie S1). Considering the kinetics, the most likely instability for nanotubes is the collapse. The bending stiffness (K_b) of planar Sc_2C was calculated using $E_{diff} = K_b/(2r^2)$,[51] in which E_{diff} is the energy difference per unit area between planar and circular Sc_2C and r is the radius of circular Sc_2C. By fitting the relation between E_{diff} and r (Figure S2b), the calculated K_b of planar Sc_2C is 3.75 ± 0.10 eV. Previous work demonstrated that the single-wall carbon nanotube exists at a maximum diameter of 2.6 nm, in which the energy for a round and collapsed nanotubes is the same.[52] Since the bending stiffness of planar Sc_2C is much larger than that (1.4 eV) of planar graphene,[53] it can be inferred that the investigated MNTs (diameter ranging from 0.9 to 2.3 nm) in this work would not collapse.

Structural Integrity of Planar Sc_2C and MNTs under Electromechanical Loads. Structural integrity is of fundamental importance for applications, and the structural integrities of planar Sc_2C and MNTs upon charge injection were examined by performing mechanical tests. The thickness of 5.6 Å was adopted for planar Sc_2C, which is obtained from the interlayer spacing of bilayer Sc_2C (Figure S3a). First, uniaxial tensile tests of charge-injected planar Sc_2C were performed along the armchair and zigzag directions (Figure S3b), respectively, which indicate that the maximum charge injection for planar Sc_2C maintaining sufficient structural integrity (no phase transition and strain to failure ≥1%) is 0.20 e/atom. From the stress−strain curves in Figure S3b, it is noted that the Young's modulus of planar Sc_2C is reduced by charge injection. The Young's modulus of pristine planar Sc_2C is calculated to be 204 GPa on the average. Upon charge injection of 0.20 e/atom, the determined Young's modulus decreases to 37.5 GPa on the average. Similarly, the maximum charge injections of MNT-6, MNT-10, and MNT-14 are determined as 0.14, 0.12, and 0.11 e/atom, respectively (Figure S3d), and the charge-injected MNTs can maintain sufficient structural integrity below the maximum charge injection. Additionally, comparing with the Young's modulus (132.8 GPa) of pristine MNT-6, the Young's moduli (122.5 and 106.5 GPa) of MNT-6 upon charge injection of 0.06 and 0.14 e/atom decrease by 7.8% and 19.8%, respectively. These results demonstrate the softening of planar Sc_2C and MNTs by charge injection because of the depletion of electrons (hole injection) that weakens the chemical bonds.

Furthermore, the electron localization function (ELF) graphs of MNT-14 and planar Sc_2C before and after charge injection are plotted in Figure 2a,b. Before charge injection, strong electron localizations with a high ELF value (0.8−0.9) occur around Sc and C atoms of MNT-14 (planar Sc_2C), indicating the ionic binding of Sc−C bonds. After charge injection, the strong electron localizations around Sc and C atoms show a little change. For further discerning of the bonding characteristics between Sc and C atoms, the Bader charge analysis was conducted.[54] Before charge injection, Sc and C atoms of planar Sc_2C lose and gain 1.203 and 2.406 electrons on the average, respectively. When 0.20 e/atom is injected, Sc and C atoms lose and gain 1.466 and 2.332 electrons on the average, respectively. For pristine MNT-14, the Sc atom in the inner and outer atomic layers loses 1.057 and 1.313 electrons on the average, respectively, and each C

https://doi.org/10.1021/acs.jpcc.1c07453
J. Phys. Chem. C 2021, 125, 25275−25283

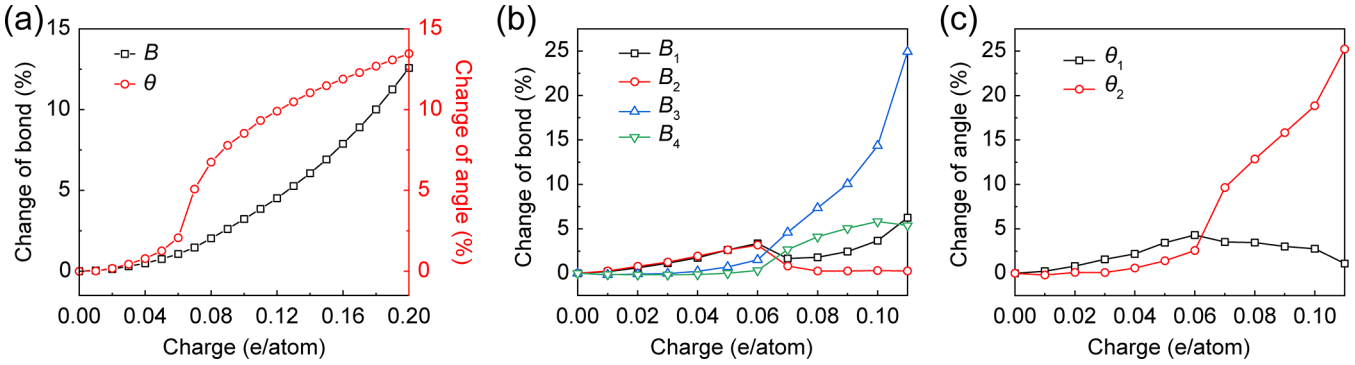

Figure 3. Evolution of interatomic parameters for (a) planar Sc_2C and (b,c) MNT-14 as functions of charge injection. Change in (b) bond length (B_{1-4}) and (c) angle (θ_{1-2}) of an MNT-14 upon charge injection.

atom gains 2.370 electrons. The different charge transfer of atoms in the inner and outer atomic layers is caused by the bending of the MNTs. After charge injection (0.11 e/atom), the Sc atom in the inner and outer atomic layers loses 1.302 and 1.445 electrons on the average, respectively, and each C atom gains 2.417 electrons. Although the electron localization between Sc and C atoms shows a slight change upon charge injection, the distance between Sc and C atoms significantly increases, indicating that the bonds (Sc−C) are weakened by charge injection. Notably, as shown in Figure 2a,b, before charge injection, electron localization with the medium ELF value also occurs between Sc atoms in the same atomic layer, indicating the covalent bonding between Sc atoms. After charge injection, the electron localization in MNT-14 (planar Sc_2C) between Sc atoms shows a reduction, suggesting the weaker covalent binding between Sc atoms than that before charge injection. Hence, it can be concluded that the softening of planar Sc_2C and MNTs by charge injection should be attributed to the weakened chemical bonds.

Electromechanical Actuation Performance. Next, we investigate the electromechanical actuation performance of MNTs upon charge injection. Notably, only hole injection was explored in this work since it was found that materials upon hole injection exhibit higher actuation performance than that upon electron injection.[10,16] The actuation performance of MNTs is characterized by the radial and axial strain that are defined as the changes in D and L for MNTs upon charge injection divided by the values of D and L for pristine MNTs, respectively. Similarly, the actuation strain of planar Sc_2C is characterized as the change of in-plane lattice parameters after charge injection divided by their corresponding original values before charge injection. First, both the radial and axial strain of MNT-14 increase with increasing charge injection. Afterward, the radial actuation strain is increasingly larger than the axial actuation strain as the charge injection exceeds 0.04 e/atom. Finally, the axial strain drops as the charge injection exceeds 0.10 e/atom (Figure 2c and Movie S2). Upon a maximum charge injection of 0.11 e/atom, the radial and axial strain of MNTs reach 26.8% and 7.8%, respectively, indicating significant anisotropic actuation performance. In sharp contrast, planar Sc_2C exhibits an in-plane isotropic actuation strain of 11.0% upon charge injection of 0.11 e/atom, and the maximum actuation strain of planar Sc_2C is as high as 23.5%, when the hole of 0.20 e/atom is injected (Figure 2d). Additionally, we find that the radial actuation strain of MNT-6 and MNT-10 are lower than that of MNT-14 upon the same amount of charge injection (Figure S4a), indicating that the increase in bending curvature would limit the radial actuation of MNTs.

Mechanism for High Electromechanical Actuation Performance. To uncover the underlying mechanism behind the electromechanical actuation performance of the planar Sc_2C and MNTs, we track their interatomic parameters in response to charge injection. The evolution of interatomic parameters is explored (Figures 3 and S4b−e). As shown in Figure 3a, the interatomic parameters of planar Sc_2C increase with increasing charge injection. The isotropic actuation strain of planar Sc_2C can be derived as functions of the interatomic parameters[16]

$$\varepsilon = \frac{B \sin(\theta/2)}{B_0 \sin(\theta_0/2)} - 1 \tag{1}$$

where B_0 (B) and θ_0 (θ) are the bond length and angle of planar Sc_2C before (after) charge injection, respectively. By substituting the interatomic parameters (B and θ) into eq 1, the obtained actuation strain is found to be consistent with the directly measured values (Figure 2d). Because of bending-induced symmetry breakdown, eq 1 is no longer applicable for MNTs. Compared with the change in bond length and angle in planar Sc_2C (Figure 3a), the change in bond length and angle in MNTs is very different (Figures 3b,c and S4b−e), resulting from the bending-induced symmetry breakdown of MNTs. As a small amount of hole is injected (less than 0.04 e/atom), Figure 3b shows that B_1 and B_2 slightly elongate (~1.2%), while B_3 and B_4 slightly shorten (~0.18%), and Figure 3c shows that the change of θ_1 (~1.6%) is larger than that (~0.08%) of θ_2. Hence, the very small actuation strain of MNT-14 upon a small amount of charge injection (less than 0.04 e/atom) is dominated by the changes in B_1, B_2, and θ_1. As charge injection increases, B_3 and θ_2 significantly increase. When charge injection increases to 0.11 e/atom, the changes of B_3 and θ_2 reach about 24.9% and 25.2%, respectively, which are much larger than the change of other parameters. Hence, the maximum actuation performance of MNT-14 is dominated by the elongation of B_3 in the outer atomic layer and the change of θ_2 in the inner atomic layer (Figure 1d). Additionally, the structural change of MNT-6 and MNT-10 as functions of charge injection (Figure S4b−e) exhibits similar evolution of interatomic parameters for these MNTs upon charge injection. The difference in radial actuation strain of MNTs with different diameters results from the change in interatomic parameters (Figures 3b,c and S4b−e). As the charge injection increases to above 0.04 e/atom, the change in interatomic parameters (especially B_3 and θ_2) of MNTs with a

https://doi.org/10.1021/acs.jpcc.1c07453
J. Phys. Chem. C 2021, 125, 25275−25283

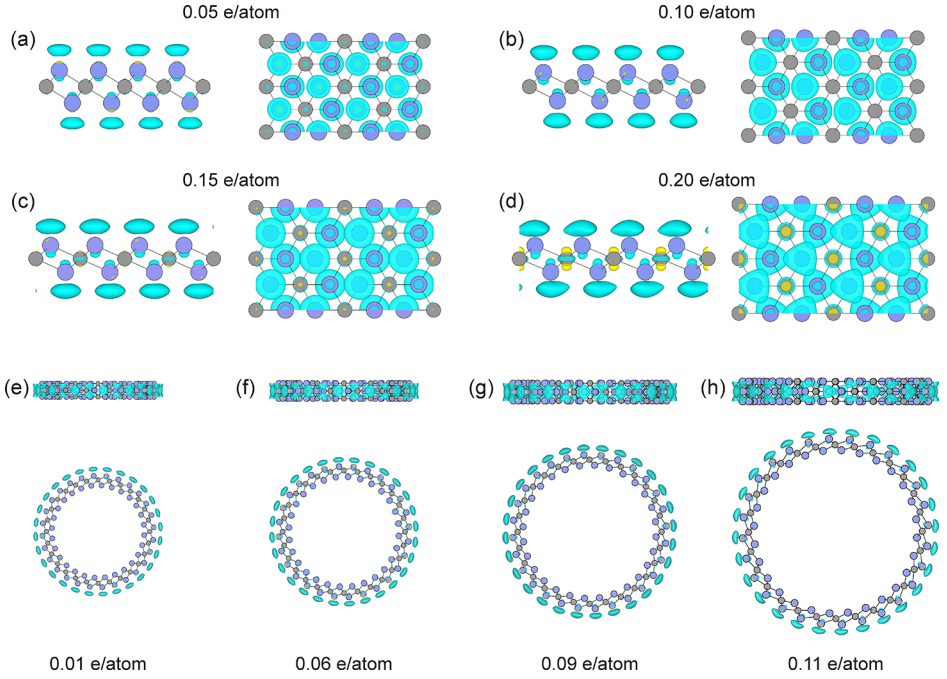

Figure 4. Top (up) and side (down) views of the excess charge density distribution of planar Sc_2C and MNT-14. (a–d) Excess charge density distribution of charge-injected planar Sc_2C with the injection amount of (a) 0.05, (b) 0.10, (c) 0.15, and (d) 0.20 e/atom is plotted, and the corresponding iso-surface values are 0.0008, 0.0015, 0.0018, and 0.0018 e/Bohr^3, respectively. Panels (e–h) are the excess charge density distribution of MNT-14 upon charge injection of (e) 0.01, (f) 0.06, (g) 0.09, and (h) 0.11 e/atom with isosurface values of 0.000195, 0.00145, 0.00165, and 0.001845 e/Bohr^3, respectively. The yellow and blue colors represent excess electron and hole, respectively.

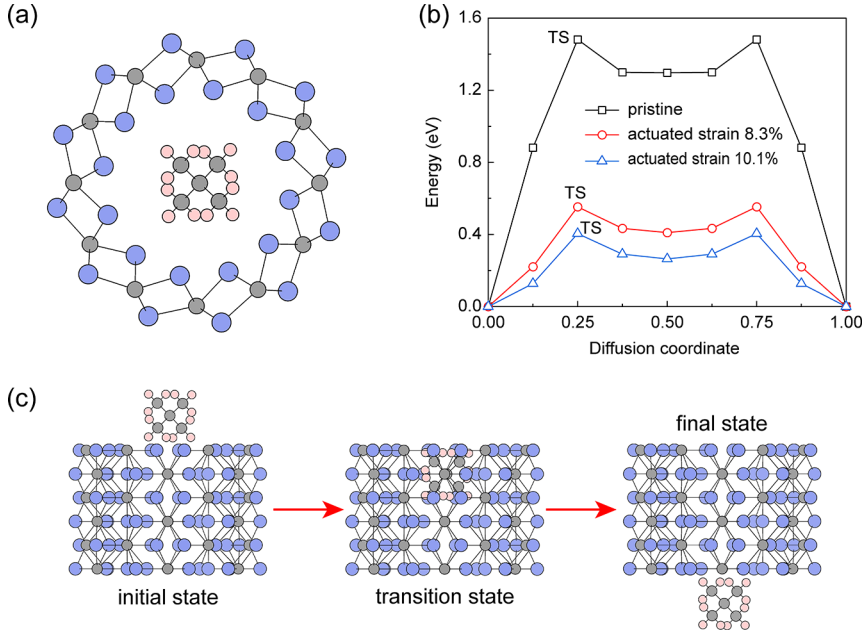

Figure 5. MNT actuator for tunable mass transport. (a) Structures of an MNT-6 and a C_5H_{12}. The pink spheres represent H atoms. (b) Energy profiles of C_5H_{12} passing through a pristine and an electromechanically actuated MNT-6. (c) Atomic configurations of C_5H_{12} through MNT-6 at the diffusion coordinates of 0.00, 0.25, and 1.00 in (b).

large diameter is larger than that of MNTs with a small diameter, which results in the obvious difference in radial actuation strain for MNTs with different diameters.

To further explore the source of the electromechanical actuation performance upon charge injection, the excess charge density distribution of planar Sc_2C and MNT-14 was calculated (Figure 4). Even upon a small amount of charge injection (0.01 e/atom), both excess holes and electrons appear in the planar Sc_2C and MNT-14 (Figure S5), indicating that the intrinsic charge density distribution is perturbed.[13,16,55] For charge-injected planar Sc_2C, the excess charge density distributions are plotted in Figure 4a–d, showing that excess hole accumulates around Sc atoms both in the upper and lower atomic layers. Besides, the concentration of the excess hole around Sc atoms increases with increasing charge injection. Notably, compared with

https://doi.org/10.1021/acs.jpcc.1c07453
J. Phys. Chem. C 2021, 125, 25275–25283

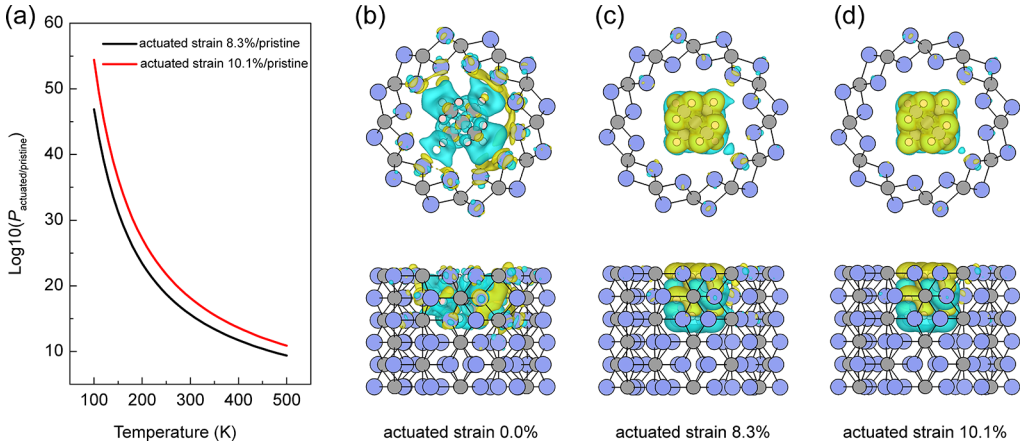

Figure 6. (a) Logarithmic scale for the relative C_5H_{12} transport rates across an electromechanically actuated MNT-6. Side and top views of the charge density difference of one C_5H_{12} through (b) pristine and (c,d) electromechanically actuated MNT-6 at the TS with an isosurface value of 0.0015 e/Bohr^3. Herein, charge density difference of a C_5H_{12} through actuated MNT-6 with the radial actuation strains of (c) 8.3 and (d) 10.1% is plotted. Color coding consists of yellow for charge gain and green for charge loss.

excess charge density distribution of charge-injected planar Sc_2C, the significant difference of charge-injected MNT-14 is that most of the excess hole accumulates in the outer atomic layer (Figure 4e,f). This significant difference between the inner and outer atomic layers of MNTs is supported by the above Bader charge analysis, showing that the Sc atom in the outer atomic layer loses more electrons than that in the inner atomic layer. Due to most of the excess hole distributed atop the outer atomic layer, the repulsive Coulomb interactions caused by the excess hole−hole pairs are mainly reflected on the outer atomic layer of the MNTs, resulting in radial actuation strain. Meanwhile, since the chemical binding connections exist between the inner and outer atomic layers, the change of interatomic parameters in the outer atomic layer would cause the change in the interatomic parameters in the inner atomic layer. From Figure 3b,c, the interatomic parameters with significant change are B_3 and θ_2 that belong to the outer and inner atomic layers, respectively. In summary, on the one hand, the excess hole accumulate between Sc atoms of the planar Sc_2C and MNTs (Figure 4) can result in repulsive Coulomb interaction, which largely explain the actuation strain. On the other hand, the depletion of electron (hole injection) can soften planar Sc_2C and MNTs (see Structural Integrity of Planar Sc_2C and MNTs under Electromechanical Loads for details). Therefore, the electromechanical actuation performance of planar Sc_2C and MNTs is attributed to the Coulomb interaction of excess charge and softening of structures.

Potential Applications of MNT Actuators. At present, the existing nanochannels meet challenges in terms of stimulus complexity (e.g., solutions and ions) and response uncontrollability (e.g., low durability and response rate).[36] Considering the high electromechanical actuation performance, we propose potential uses of MNTs as tunable nanochannels and demonstrate this application by passing a molecule (neopentane, C_5H_{12}) through MNT-6 with various actuated diameters. The diameter of pristine MNT-6 is 0.9 nm, and the kinetic diameter of the C_5H_{12} molecule is 0.6 nm.[56] The atomic configuration of MNT-6 with C_5H_{12} placed on its axial line is depicted in Figure 5a. For the calculation of C_5H_{12} passing through an electromechanically actuated MNT-6, a vacuum layer of 30 Å was used. The energy barrier (ΔE) for C_5H_{12} passing through pristine and electromechanically actuated MNT-6 was calculated along the axial direction (Figure 5b), which is defined by[57]

$$\Delta E = E_{TS} - E_{SS} \tag{2}$$

where E_{TS} and E_{SS} are the total energies of the transition state (TS) and stable state (SS) of C_5H_{12} across electromechanically actuated MNT-6, respectively. The atomic configurations at the initial, transition, and final states are illustrated in Figure 5c. Before charge injection, the energy barrier is determined as 1.48 eV, indicating that C_5H_{12} cannot pass through pristine MNT-6 at a moderate temperature and pressure.[58] Afterward, the energy barriers of C_5H_{12} passing through an actuated MNT-6 with the equivalent radial actuation strains of 8.3% and 10.1% (corresponding to charge injections of 0.10 and 0.11 e/atom, respectively, as shown in Figure S4a) are determined as 0.55 and 0.40 eV (Figure 5b), respectively. Compared with that (1.48 eV) passing through pristine MNT-6, these much lower energy barriers (0.40−0.55 eV) suggest that the C_5H_{12} molecule can easily pass through an actuated MNT-6 at a moderate temperature and pressure.[58]

Furthermore, we quantify the transport rates of a C_5H_{12} molecule passing through an electromechanically actuated MNT-6 by using the Arrhenius equation[59]

$$R = Ae^{-\Delta E/k_BT} \tag{3}$$

where R, A, k_B, and T are the transport rate, prefactor, Boltzmann constant, and absolute temperature, respectively. The prefactor is identical for one molecule.[60,61] Based on eq 3, the relative transport rate of a C_5H_{12} through an electromechanically actuated MNT-6 compared with that through a pristine MNT-6 is derived as

$$P_{\text{actuated/pristine}} = \frac{Ae^{-\Delta E/k_BT}}{Ae^{-\Delta E_0/k_BT}} = e^{(\Delta E_0 - \Delta E)/k_BT} \tag{4}$$

where ΔE_0 and ΔE are the energy barriers of C_5H_{12} passing through a pristine and an actuated MNT-6, respectively. Accordingly, the relative transport rates as functions of temperature were calculated as shown in Figure 6a, indicating the tunability of transport rates across multiscales. For example, the transport rate of C_5H_{12} passing through MNT-6 upon charge injection of 0.11 e/atom is 18 orders of

https://doi.org/10.1021/acs.jpcc.1c07453
J. Phys. Chem. C 2021, 125, 25275−25283

magnitude higher than that passing through a pristine MNT-6 at 300 K. Hence, the tunability of the sieving diameters of MNTs is promising for tunable mass transport.

To further clarify the reason for the reduced barrier, in the following, we analyze the charge density difference of one C_5H_{12} through MNT-6 at the TS. The charge density difference ($\Delta\rho$) is defined as

$$\Delta\rho = \rho_{tot} - \rho_{MNT\text{-}6} - \rho_{C_5H_{12}} \quad (5)$$

where ρ_{tot}, $\rho_{MNT\text{-}6}$, and ρ_{C5H12} are the charge densities of MNT-6 with one C_5H_{12}, MNT-6, and C_5H_{12}, respectively. The charge density difference is plotted in Figure 6b–d. Before charge injection, there is considerable charge overlap between C_5H_{12} and pristine MNT-6 (Figure 6b), indicating that C_5H_{12} is strongly pinned on the inner atomic layer of pristine MNT-6. This observation is consistent with the Bader charge analysis, which reveals that the total charge transfer between C_5H_{12} and pristine MNT-6 is 0.827 electrons. As shown in Figure 6c,d, the interaction of C_5H_{12} with actuated MNT-6 is reduced, which is caused by the actuated diameter. The Bader charge analysis demonstrates that the charge transfer between a C_5H_{12} molecule and an electromechanically actuated MNT-6 decreases as the actuated diameter increases. The calculated charge transfer between C_5H_{12} and actuated MNT-6 with the radial actuation strains of 8.3% and 10.1% is 0.615 and 0.575 electrons, respectively. These results suggest that the actuated diameter of MNTs can effectively reduce the charge transfer between C_5H_{12} and MNTs at the TS and hence eventually reduce the energy barrier.

CONCLUSIONS

In summary, this work computationally demonstrate that MNTs exhibit high electromechanical actuation performance while maintaining sufficient structural integrity under a certain amount of charge injection. The maximum radial actuation strain of MNTs is as high as 26.8%. The underlying mechanism is elucidated by analysis through atomic- and electronic-scales. Finally, we explore the potential use of electromechanically actuated MNTs as tunable nanochannels by demonstrating the passage of a molecule (C_5H_{12}) through an MNT with various actuated dimeters, indicating the tunability of transport rates across multiscales at a wide range of temperatures.

ASSOCIATED CONTENT

Supporting Information

The Supporting Information is available free of charge at https://pubs.acs.org/doi/10.1021/acs.jpcc.1c07453.

Illustrations of MNT-6 and MNT-10 structures and convergence test for the selected energy cutoff, temperature and system energy during AIMD simulations, calculations for the bending stiffness of planar Sc_2C, mechanical tests for MNTs and planar Sc_2C under the combined electromechanical loads, electromechanical actuation strain of MNT-6 and MNT-10 and their corresponding change of interatomic parameters, and excess charge density distribution of planar Sc_2C and MNT-14 upon 0.01 e/atom injection (PDF)

AIMD simulations of MNT-14 at 298 K for 10 ps (MP4)

MNT-14 upon charge injection (MP4)

AUTHOR INFORMATION

Corresponding Authors

Ze Liu − *Department of Engineering Mechanics, School of Civil Engineering, Wuhan University, Wuhan, Hubei 430072, China;* orcid.org/0000-0002-9906-5351; Email: ze.liu@whu.edu.cn

Enlai Gao − *Department of Engineering Mechanics, School of Civil Engineering, Wuhan University, Wuhan, Hubei 430072, China;* orcid.org/0000-0003-1960-0260; Email: enlaigao@whu.edu.cn

Authors

Bozhao Wu − *Department of Engineering Mechanics, School of Civil Engineering, Wuhan University, Wuhan, Hubei 430072, China*

Yuanpeng Yao − *Department of Engineering Mechanics, School of Civil Engineering, Wuhan University, Wuhan, Hubei 430072, China*

Ke Zhou − *State Key Laboratory for Strength and Vibration of Mechanical Structures, School of Aerospace Engineering, Xi'an Jiaotong University, Xi'an 710049, China;* orcid.org/0000-0003-2239-4381

Complete contact information is available at: https://pubs.acs.org/10.1021/acs.jpcc.1c07453

Author Contributions

§B.W. and Y.Y. contribute equally.

Notes

The authors declare no competing financial interest.

ACKNOWLEDGMENTS

This work was supported by the Wuhan Science and Technology Bureau of China (2019010701011390). The numerical calculations in this work were performed on a supercomputing system in the Supercomputing Center of Wuhan University.

REFERENCES

(1) Ryabchun, A.; Li, Q.; Lancia, F.; Aprahamian, I.; Katsonis, N. Shape-Persistent Actuators from Hydrazone Photoswitches. *J. Am. Chem. Soc.* **2019**, *141*, 1196−1200.

(2) Li, M.; Wang, X.; Dong, B.; Sitti, M. In-Air Fast Response and High Speed Jumping and Rolling of a Light-Driven Hydrogel Actuator. *Nat. Commun.* **2020**, *11*, 3988.

(3) Sun, W.-J.; Guan, Y.; Wang, Y.-Y.; Wang, T.; Xu, Y.-T.; Kong, W.-W.; Jia, L.-C.; Yan, D.-X.; Li, Z.-M. Low-Voltage Actuator with Bilayer Structure for Various Biomimetic Locomotions. *ACS Appl. Mater. Interfaces* **2021**, *13*, 43449−43457.

(4) Zhao, Y.; et al. Somatosensory Actuator Based on Stretchable Conductive Photothermally Responsive Hydrogel. *Sci. Robot.* **2021**, *6*, No. eabd5483.

(5) Mirvakili, S. M.; Hunter, I. W. Artificial Muscles: Mechanisms, Applications, and Challenges. *Adv. Mater.* **2018**, *30*, 1704407.

(6) Jiang, T. Y.; Ng, T. Y.; Lam, K. Y. Optimization of a Piezoelectric Ceramic Actuator. *Sens. Actuators, A* **2000**, *84*, 81−94.

(7) Baughman, R. H.; Cui, C.; Zakhidov, A. A.; Iqbal, Z.; Barisci, J. N.; Spinks, G. M.; Wallace, G. G.; Mazzoldi, A.; De Rossi, D.; Rinzler, A. G.; Jaschinski, O.; Roth, S.; Kertesz, M. Carbon Nanotube Actuators. *Science* **1999**, *284*, 1340−1344.

(8) Sun, G.; Kürti, J.; Kertesz, M.; Baughman, R. H. Dimensional Changes as a Function of Charge Injection in Single-Walled Carbon Nanotubes. *J. Am. Chem. Soc.* **2002**, *124*, 15076−15080.

(9) Rogers, G. W.; Liu, J. Z. Graphene Actuators: Quantum-Mechanical and Electrostatic Double-Layer Effects. *J. Am. Chem. Soc.* **2011**, *133*, 10858−10863.

(10) Rogers, G. W.; Liu, J. Z. High-Performance Graphene Oxide Electromechanical Actuators. *J. Am. Chem. Soc.* **2012**, *134*, 1250−1255.
(11) Si, C.; Duan, W.; Liu, Z.; Liu, F. Electronic Strengthening of Graphene by Charge Doping. *Phys. Rev. Lett.* **2012**, *109*, 226802.
(12) Chang, Z.; Deng, J.; Chandrakumara, G. G.; Yan, W.; Liu, J. Z. Two-Dimensional Shape Memory Graphene Oxide. *Nat. Commun.* **2016**, *7*, 11972.
(13) Wu, B.; Deng, H.-X.; Jia, X.; Shui, L.; Gao, E.; Liu, Z. High-Performance Phosphorene Electromechanical Actuators. *npj Comput. Mater.* **2020**, *6*, 27.
(14) Van Thanh, V.; Hung, N. T.; Van Truong, D. Charge-Induced Electromechanical Actuation of Mo- and W-Dichalcogenide Monolayers. *RSC Adv.* **2018**, *8*, 38667−38672.
(15) Chen, K.; Deng, J.; Shi, Q.; Ding, X.; Sun, J.; Yang, S.; Liu, J. Z. Charge Doping Induced Reversible Multistep Structural Phase Transitions and Electromechanical Actuation in Two-Dimensional 1T′-MoS_2. *Nanoscale* **2020**, *12*, 12541−12550.
(16) Wu, B.; Cai, X.; Shui, L.; Gao, E.; Liu, Z. Extraordinary Electromechanical Actuation of Ti_2C MXene. *J. Phys. Chem. C* **2021**, *125*, 1060−1068.
(17) Cao, J.; Zhou, Z.; Song, Q.; Chen, K.; Su, G.; Zhou, T.; Zheng, Z.; Lu, C.; Zhang, X. Ultrarobust $Ti_3C_2T_x$ MXene-Based Soft Actuators Via Bamboo-Inspired Mesoscale Assembly of Hybrid Nanostructures. *ACS Nano* **2020**, *14*, 7055−7065.
(18) Pang, D.; Alhabeb, M.; Mu, X.; Dall'Agnese, Y.; Gogotsi, Y.; Gao, Y. Electrochemical Actuators Based on Two-Dimensional $Ti_3C_2T_x$ (MXene). *Nano Lett.* **2019**, *19*, 7443−7448.
(19) Bunch, J. S.; van der Zande, A. M.; Verbridge, S. S.; Frank, I. W.; Tanenbaum, D. M.; Parpia, J. M.; Craighead, H. G.; McEuen, P. L. Electromechanical Resonators from Graphene Sheets. *Science* **2007**, *315*, 490−493.
(20) Naguib, M.; Kurtoglu, M.; Presser, V.; Lu, J.; Niu, J.; Heon, M.; Hultman, L.; Gogotsi, Y.; Barsoum, M. W. Two-Dimensional Nanocrystals Produced by Exfoliation of Ti_3AlC_2. *Adv. Mater.* **2011**, *23*, 4248−4253.
(21) Enyashin, A. N.; Ivanovskii, A. L. Atomic Structure, Comparative Stability and Electronic Properties of Hydroxylated Ti_2C and Ti_3C_2 Nanotubes. *Comput. Theor. Chem.* **2012**, *989*, 27−32.
(22) Zhang, X.; Ma, Z.; Zhao, X.; Tang, Q.; Zhou, Z. Computational Studies on Structural and Electronic Properties of Functionalized MXene Monolayers and Nanotubes. *J. Mater. Chem. A* **2015**, *3*, 4960−4966.
(23) Li, B.; Wang, C.; Zhang, Y.; Wang, Y. High CO_2 Absorption Capacity of Metal-Based Ionic Liquids: A Molecular Dynamics Study. *Green Energy Environ.* **2021**, *6*, 253−260.
(24) Liu, L.; Wang, L.; Liu, D.; Yang, Q.; Zhong, C. High-Throughput Computational Screening of Cu-MOFs with Open Metal Sites for Efficient C_2H_2/C_2H_4 Separation. *Green Energy Environ.* **2020**, *5*, 333−340.
(25) Wang, J.; Zhou, M.; Lu, D.; Fei, W.; Wu, J. Computational Screening and Design of Nanoporous Membranes for Efficient Carbon Isotope Separation. *Green Energy Environ.* **2020**, *5*, 364−373.
(26) Ge, L.; Wu, J.; Wang, C.; Zhang, F.; Liu, Z. Engineering Artificial Switchable Nanochannels for Selective Monitoring of Nitric Oxide Release from Living Cells. *Biosens. Bioelectron.* **2020**, *169*, 112606.
(27) Chen, Y.; Li, X.; Wang, M.; Peng, L.; Yu, Z.; Peng, X.; Song, J.; Qu, J. Virus-Inspired Deformable Mesoporous Nanocomposites for High Efficiency Drug Delivery. *Small* **2020**, *16*, 1906028.
(28) Williams, E. M.; Jung, S. M.; Coffman, J. L.; Lutz, S. Pore Engineering for Enhanced Mass Transport in Encapsulin Nanocompartments. *ACS Synth. Biol.* **2018**, *7*, 2514−2517.
(29) Sharp, C. H.; Bukowski, B. C.; Li, H.; Johnson, E. M.; Ilic, S.; Morris, A. J.; Gersappe, D.; Snurr, R. Q.; Morris, J. R. Nanoconfinement and Mass Transport in Metal−Organic Frameworks. *Chem. Soc. Rev.* **2021**, *50*, 11530.
(30) Goyal, A.; Marcandalli, G.; Mints, V. A.; Koper, M. T. M. Competition between CO_2 Reduction and Hydrogen Evolution on a Gold Electrode under Well-Defined Mass Transport Conditions. *J. Am. Chem. Soc.* **2020**, *142*, 4154−4161.
(31) Teng, Y.; Liu, P.; Fu, L.; Kong, X.-Y.; Jiang, L.; Wen, L. Bioinspired Nervous Signal Transmission System Based on Two-Dimensional Laminar Nanofluidics: From Electronics to Ionics. *Proc. Natl. Acad. Sci. U.S.A.* **2020**, *117*, 16743−16748.
(32) Chen, W.; et al. Improved Ion Transport in Hydrogel-Based Nanofluidics for Osmotic Energy Conversion. *ACS Cent. Sci.* **2020**, *6*, 2097−2104.
(33) Wu, Y.; et al. Proton Transport Enabled by a Field-Induced Metallic State in a Semiconductor Heterostructure. *Science* **2020**, *369*, 184−188.
(34) Hou, P.; Li, D.; Yang, N.; Wan, J.; Zhang, C.; Zhang, X.; Jiang, H.; Zhang, Q.; Gu, L.; Wang, D. Delicate Control on the Shell Structure of Hollow Spheres Enables Tunable Mass Transport in Water Splitting. *Angew. Chem.* **2021**, *133*, 7002−7007.
(35) Siwy, Z. S.; Howorka, S. Engineered Voltage-Responsive Nanopores. *Chem. Soc. Rev.* **2010**, *39*, 1115−1132.
(36) Wang, C.; Wang, D.; Miao, W.; Shi, L.; Wang, S.; Tian, Y.; Jiang, L. Bioinspired Ultrafast-Responsive Nanofluidic System for Ion and Molecule Transport with Speed Control. *ACS Nano* **2020**, *14*, 12614−12620.
(37) Li, Y.; Tu, L.; Ma, X.; Chen, H.; Fan, Y.; Zhou, Q.; Sun, Y. Engineering a Smart Nanofluidic Sensor for High-Performance Peroxynitrite Sensing through a Spirocyclic Ring Open/Close Reaction Strategy. *ACS Sens.* **2021**, *6*, 808−814.
(38) Yameen, B.; Ali, M.; Neumann, R.; Ensinger, W.; Knoll, W.; Azzaroni, O. Ionic Transport through Single Solid-State Nanopores Controlled with Thermally Nanoactuated Macromolecular Gates. *Small* **2009**, *5*, 1287−1291.
(39) Lopez, L. G.; Nap, R. J. Highly Sensitive Gating in pH-Responsive Nanochannels as a Result of Ionic Bridging and Nanoconfinement. *Phys. Chem. Chem. Phys.* **2018**, *20*, 16657−16665.
(40) Zhang, Z.; et al. Bioinspired Graphene Oxide Membranes with pH-Responsive Nanochannels for High-Performance Nanofiltration. *ACS Nano* **2021**, *15*, 13178−13187.
(41) Tian, Y.; Hou, X.; Wen, L.; Guo, W.; Song, Y.; Sun, H.; Wang, Y.; Jiang, L.; Zhu, D. A Biomimetic Zinc Activated Ion Channel. *Chem. Commun.* **2010**, *46*, 1682−1684.
(42) Jiang, Y.; Liu, N.; Guo, W.; Xia, F.; Jiang, L. Highly-Efficient Gating of Solid-State Nanochannels by DNA Supersandwich Structure Containing ATP Aptamers: A Nanofluidic Implication Logic Device. *J. Am. Chem. Soc.* **2012**, *134*, 15395−15401.
(43) Qian, T.; Zhang, H.; Li, X.; Hou, J.; Zhao, C.; Gu, Q.; Wang, H. Efficient Gating of Ion Transport in Three-Dimensional Metal−Organic Framework Sub-Nanochannels with Confined Light-Responsive Azobenzene Molecules. *Angew. Chem., Int. Ed.* **2020**, *59*, 13051−13056.
(44) Kresse, G.; Furthmüller, J. Efficiency of Ab-Initio Total Energy Calculations for Metals and Semiconductors Using a Plane-Wave Basis Set. *Comput. Mater. Sci.* **1996**, *6*, 15−50.
(45) Kresse, G.; Furthmüller, J. Efficient Iterative Schemes for Ab Initio Total Energy Calculations Using a Plane-Wave Basis Set. *Phys. Rev. B: Condens. Matter Mater. Phys.* **1996**, *54*, 11169.
(46) Filippi, C.; Singh, D. J.; Umrigar, C. J. All-Electron Local-Density and Generalized-Gradient Calculations of the Structural Properties of Semiconductors. *Phys. Rev. B: Condens. Matter Mater. Phys.* **1994**, *50*, 14947.
(47) Perdew, J. P.; Burke, K.; Ernzerhof, M. Generalized Gradient Approximation Made Simple. *Phys. Rev. Lett.* **1996**, *77*, 3865−3868.
(48) Blöchl, P. E. Projector Augmented-Wave Method. *Phys. Rev. B: Condens. Matter Mater. Phys.* **1994**, *50*, 17953.
(49) Grimme, S.; Antony, J.; Ehrlich, S.; Krieg, H. A Consistent and Accurate Ab Initio Parametrization of Density Functional Dispersion Correction (DFT-D) for the 94 Elements H-Pu. *J. Chem. Phys.* **2010**, *132*, 154104.
(50) Monkhorst, H. J.; Pack, J. D. Special Points for Brillouin-Zone Integrations. *Phys. Rev. B: Solid State* **1976**, *13*, 5188.

https://doi.org/10.1021/acs.jpcc.1c07453
J. Phys. Chem. C 2021, 125, 25275−25283

(51) Gao, E.; Xu, Z. Thin-Shell Thickness of Two-Dimensional Materials. *J. Appl. Mech.* **2015**, *82*, 121012.
(52) Zhang, C.; Bets, K.; Lee, S. S.; Sun, Z.; Mirri, F.; Colvin, V. L.; Yakobson, B. I.; Tour, J. M.; Hauge, R. H. Closed-Edged Graphene Nanoribbons from Large-Diameter Collapsed Nanotubes. *ACS Nano* **2012**, *6*, 6023−6032.
(53) Wei, Y.; Wang, B.; Wu, J.; Yang, R.; Dunn, M. L. Bending Rigidity and Gaussian Bending Stiffness of Single-Layered Graphene. *Nano Lett.* **2013**, *13*, 26−30.
(54) Henkelman, G.; Arnaldsson, A.; Jónsson, H. A Fast and Robust Algorithm for Bader Decomposition of Charge Density. *Comput. Mater. Sci.* **2006**, *36*, 354−360.
(55) Rogers, G. W.; Liu, J. Z. Monolayer Graphene Oxide as a Building Block for Artificial Muscles. *Appl. Phys. Lett.* **2013**, *102*, 021903.
(56) Li, J.-R.; Kuppler, R. J.; Zhou, H.-C. Selective Gas Adsorption and Separation in Metal−Organic Frameworks. *Chem. Soc. Rev.* **2009**, *38*, 1477−1504.
(57) Kozuch, S.; Shaik, S. How to Conceptualize Catalytic Cycles? The Energetic Span Model. *Acc. Chem. Res.* **2011**, *44*, 101−110.
(58) Gao, E.; Zhang, C.; Zhou, K.; Wei, N. Computational Study on Strain-Engineered Graphene Nanopores for Selective Gas Separation. *ACS Appl. Nano Mater.* **2020**, *3*, 11474−11480.
(59) Logan, S. R. The Origin and Status of the Arrhenius Equation. *J. Chem. Educ.* **1982**, *59*, 279−281.
(60) Blankenburg, S.; Bieri, M.; Fasel, R.; Müllen, K.; Pignedoli, C. A.; Passerone, D. Porous Graphene as an Atmospheric Nanofilter. *Small* **2010**, *6*, 2266−2271.
(61) Wang, Y.; Li, J.; Yang, Q.; Zhong, C. Two-Dimensional Covalent Triazine Framework Membrane for Helium Separation and Hydrogen Purification. *ACS Appl. Mater. Interfaces* **2016**, *8*, 8694−8701.

https://doi.org/10.1021/acs.jpcc.1c07453
J. Phys. Chem. C 2021, 125, 25275−25283

Supporting Information

Electromechanically Actuated MXene Nanotubes for Tunable Mass Transport

Bozhao Wu[1#], Yuanpeng Yao[1#], Ke Zhou[2], Ze Liu[1*], and Enlai Gao[1*]

[1]Department of Engineering Mechanics, School of Civil Engineering, Wuhan University, Wuhan, Hubei 430072, China.

[2]State Key Laboratory for Strength and Vibration of Mechanical Structures, School of Aerospace Engineering, Xi'an Jiaotong University, Xi'an 710049, China.

[#]These authors contribute equally.

[*]Corresponding author. Email: ze.liu@whu.edu.cn; enlaigao@whu.edu.cn

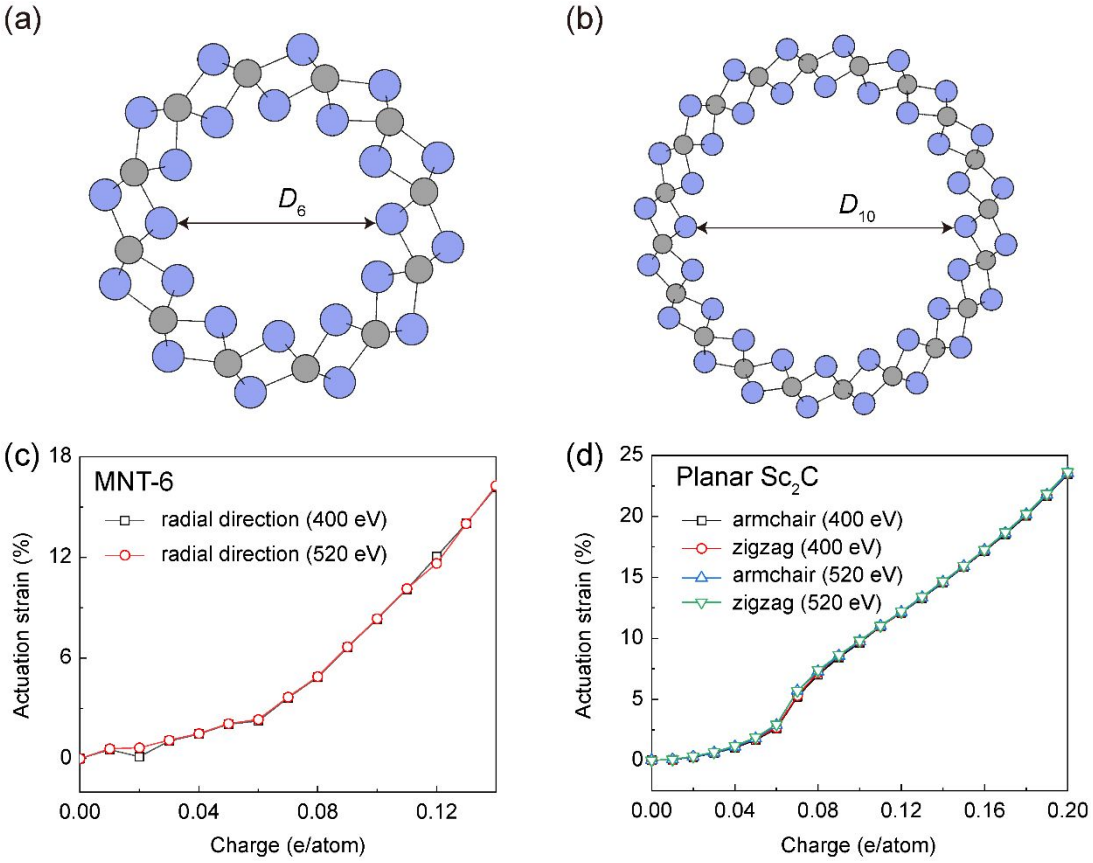

Figure S1. (a-b) Atomic configurations of (a) MNT-6 and (b) MNT-10. (c-d) Convergence tests for the energy cutoff. Evidently, the calculated actuation strains of planar Sc_2C and MNT-6 using an energy cutoff of 400 eV are almost same to that using an energy cutoff of 520 eV, indicating that the energy cutoff of 400 eV provides a good balance between computational accuracy and effort.

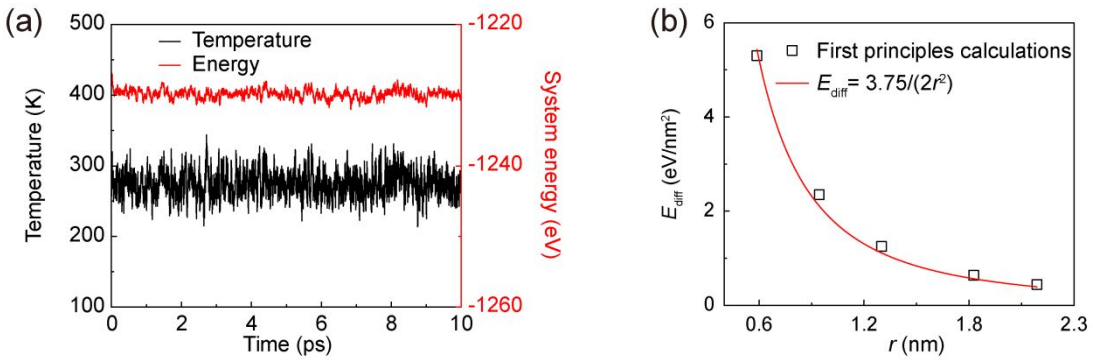

Figure S2. (a) Evolutions of temperature and system energy during AIMD simulations, which were performed at 298 K for 10 ps using Andersen thermostat to control the temperature (see Movie S1 for the animation). (b) Energy per nm^2 versus the radius (r) (herein, r is the radius of circular Sc_2C): first principles calculations data (symbols) and continuum model (red solid lines, with a bending stiffness of 3.75 eV).

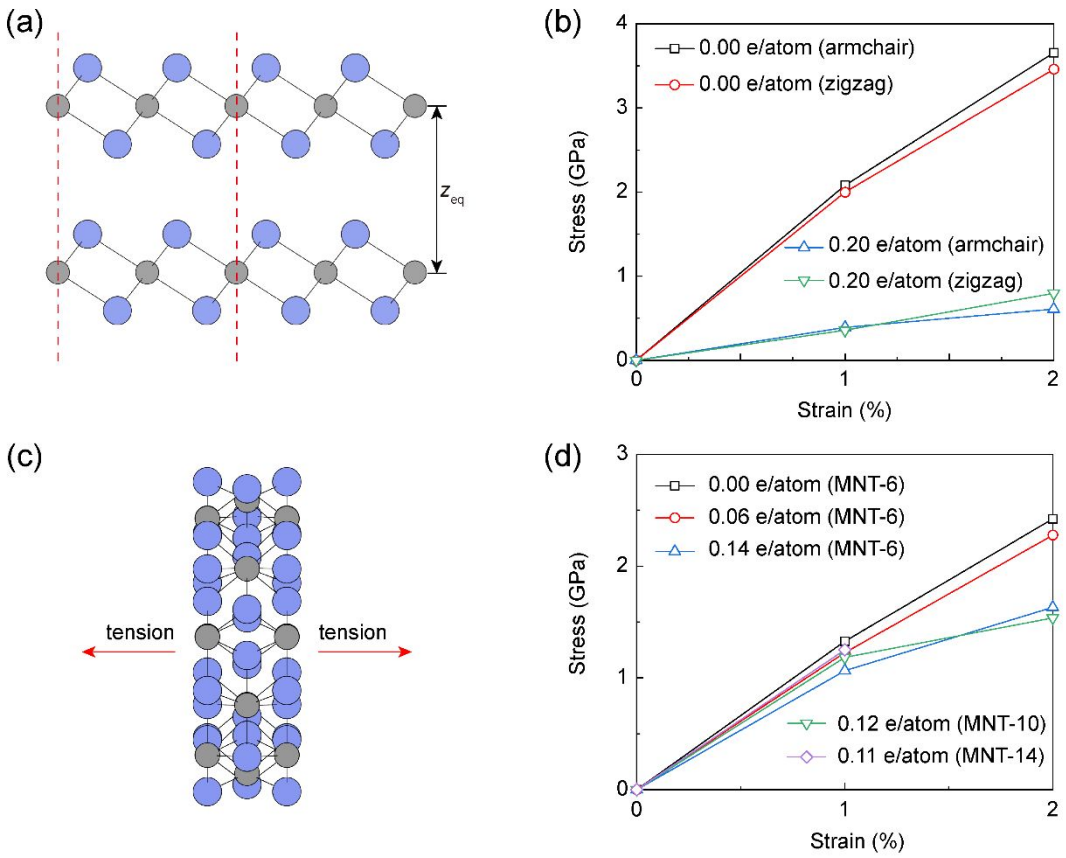

Figure S3. Structural integrity under combined electromechanical loads. (a) Bilayer Sc_2C was used to determine the interlayer spacing (z_{eq}). The unit cell is within the red dashed lines. (b) Tensile tests of planar Sc_2C upon charge injection of 0.20 e/atom. (c) Illustration of MNTs under the tension. (d) Tensile tests of MNTs upon charge injection.

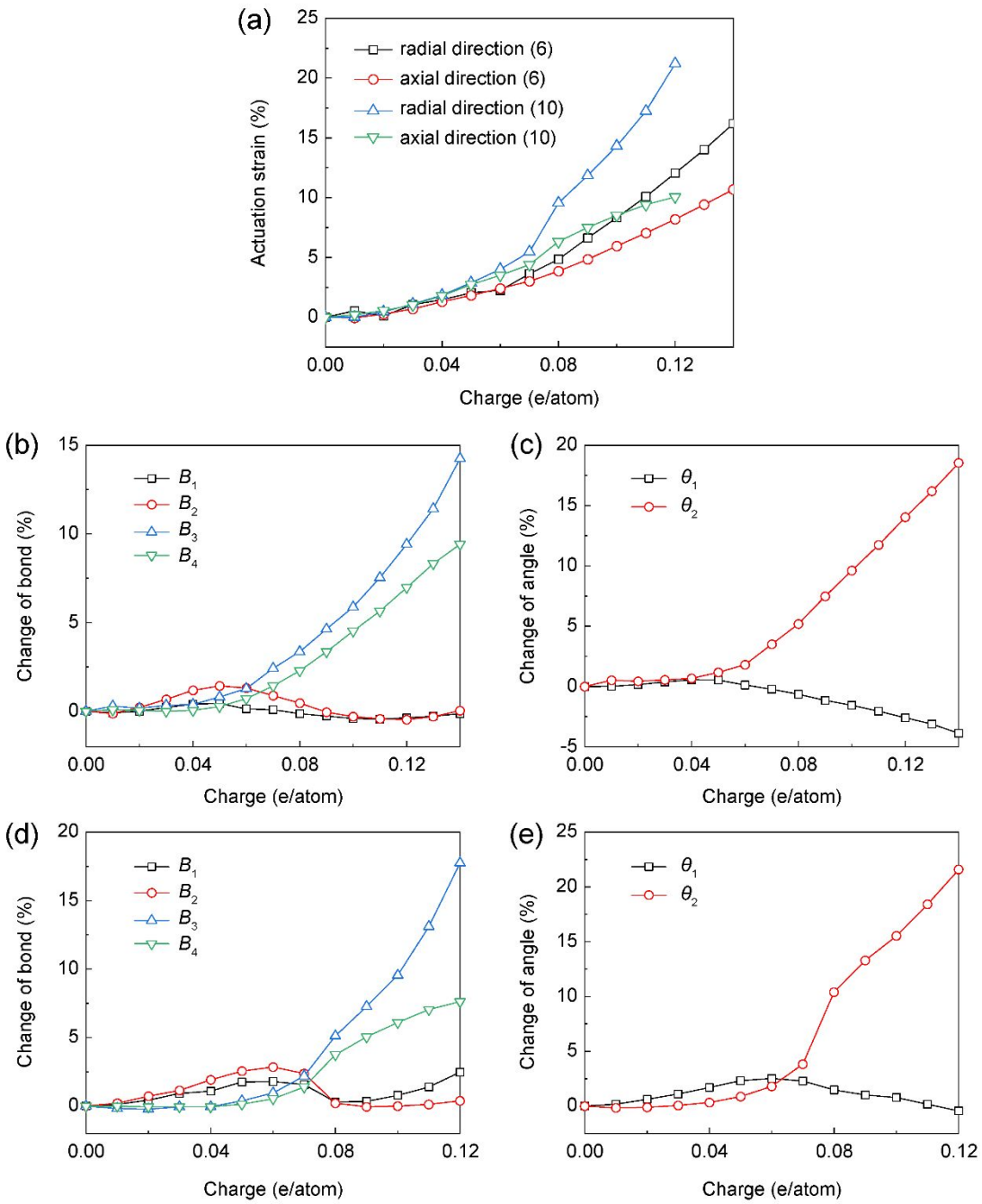

Figure S4. (a) Actuation performance of MNT-6 and MNT-10 upon charge injection. (b-e) Corresponding evolutions of the change of interatomic parameters of MNT-6 and MNT-10 as functions of charge injection. Changes of bond lengths ($B_{1\text{-}4}$) and angles ($\theta_{1\text{-}2}$) of (b-c) MNT-6 and (d-e) MNT-10 upon charge injection.

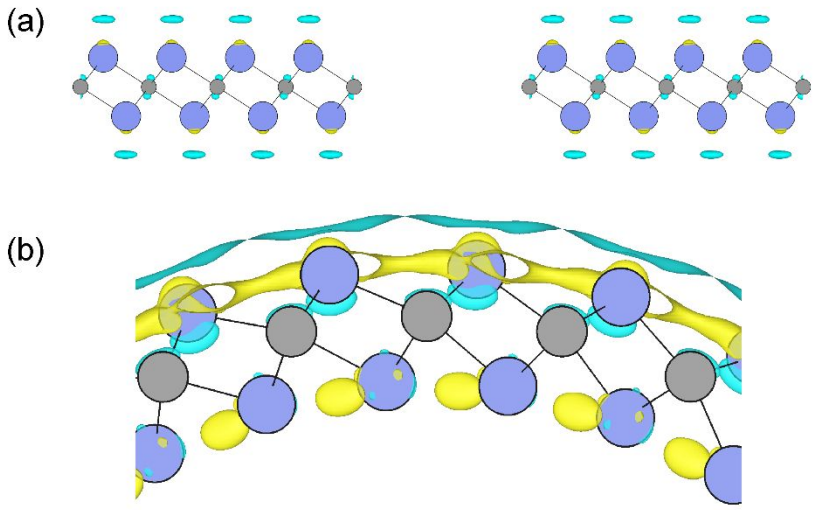

Figure S5. (a) Excess charge density distributions of (a) planar Sc_2C and (b) MNT-14 upon 0.01 e/atom injection with the iso-surface value of 0.00015 and 0.00009 e/Bohr^3, respectively. The yellow and blue colors represent excess electron and hole, respectively.

Supporting Information Movie 1:

AIMD simulations of MNT-14 at 298 K for 10 ps.

Supporting Information Movie 2:

MNT-14 upon charge injection.